Electronic Supplementary Material (ESI) for Materials Horizons.

Supporting Information: On-demand quantum spin Hall insulators controlled by two-dimensional ferroelectricity

Jiawei Huang,[1,2] Xu Duan,[3,2] Sunam Jeon,[4] Youngkuk Kim,[5] Jian Zhou,[6] Jian Li,[2,7,*] and Shi Liu[2,7,†]

[1] *Zhejiang University, Hangzhou Zhejiang 310058, P.R. China*

[2] *Key Laboratory for Quantum Materials of Zhejiang Province, School of Science, Westlake University, Hangzhou, Zhejiang 310024, China*

[3] *Fudan University, Shanghai 200433, China*

[4] *Department of Energy Science, Sungkyunkwan University, Suwon 16419, Korea*

[5] *Department of Physics Sungkyunkwan University, Suwon 16419, Korea*

[6] *Center for Alloy Innovation and Design, State Key Laboratory for Mechanical Behavior of Materials, Xi'an Jiaotong University, Xi'an 710049, China*

[7] *Institute of Natural Sciences, Westlake Institute for Advanced Study, Hangzhou, Zhejiang 310024, China*

[*] lijian@westlake.edu.cn

[†] liushi@westlake.edu.cn

I. COMPUTATIONAL METHODS

A slab model containing a vacuum layer along the z axis of at least 15 Å is used to simulate bilayer heterostructures. To better describe vdW interactions, the Grimme dispersion corrections (DFT-D3) [1] are included as well. The dipole correction in the center of the vacuum is employed to cancel the artificial electric field generated by the asymmetric slab model due to the usage of periodic boundary conditions. The in-plane lattice constants and atomic positions are fully relaxed with an energy convergence threshold of 10^{-5} Ry, a force convergence threshold of 10^{-4} Ry/Bohr, and a $8 \times 8 \times 1$ Monkhorst-Pack k-point grid for Brillouin zone sampling. We note that the dipole correction does not affect the optimized structural parameters. The GBRV ultrasoft pseudopotentials [2] are used for structural optimizations. To address the well-known issue of band gap underestimation of PBE, we compute the electronic properties such as electron affinity and work function with Heyd-Scuseria-Ernzerhof (HSE) hybrid density functional [3] using optimized norm-conserving Vanderbilt pseudopotentials [4] taken from `PseudoDojo` [5]. The HSE06 band structure with spin-orbit coupling is obtained via Wannier interpolation [6] using Wannier90 [7] interfaced with `QUANTUM ESPRESSO`, and a $4 \times 4 \times 1$ q-point grid combined with an $8 \times 8 \times 1$ k-point grid is used. The plane-wave energy and charge density cutoffs are set to 50 Ry and 250 Ry, respectively.

II. BAND BENDING DIAGRAM

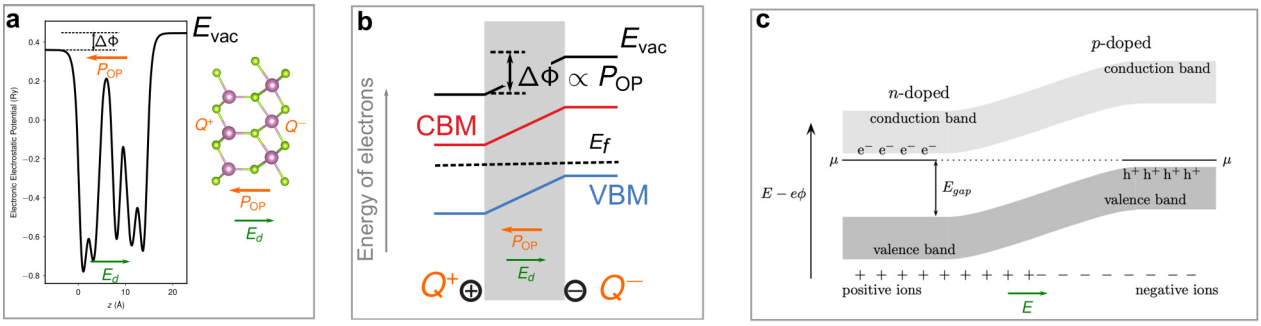

FIG. S1. (a) Electronic electrostatic potential for monolayer α-In_2Se_3 computed with DFT. Band bending in (b) a 2D ferroelectric monolayer and (c) an unbiased p-n junction (taken from page 201 of "The Oxford Solid State Physics" by Steven H. Simon.

III. GENERIC FOUR-BAND MODEL

We consider an extended BHZ model on a two-dimensional (2D) square lattice, given by

$$\begin{aligned} H(\boldsymbol{k}) = {} & a\sin k_x\Gamma_{31} + a\sin k_y\Gamma_{02} + [2b(2-\cos k_x-\cos k_y)-\lambda]\Gamma_{03} \\ & + c\Gamma_{01} + d(\cos k_x-\cos k_y)\Gamma_{12} + d\sin k_x\sin k_y\Gamma_{22}, \end{aligned} \tag{1}$$

where $\Gamma_{ij}\equiv s_i\otimes o_j$ with $s_{i=1,2,3}$ and $o_{i=1,2,3}$ the Pauli matrices for spin and orbital degrees of freedom, respectively; a, b, c and d are real positive parameters; $\boldsymbol{k}=(k_x,k_y)$ is the 2D momentum (in units of inverse lattice constant); λ is a real parameter which, in particular, represents the strength of band inversion when b is assumed to be the largest parameter (the band width) in the present problem. This Hamiltonian is time reversal invariant:

$$\mathcal{T}H(\boldsymbol{k})\mathcal{T}^{-1} = H(-\boldsymbol{k}), \quad \mathcal{T}=\mathrm{i}s_2\mathcal{K}, \tag{2}$$

where $\mathcal{T}$ is the time-reversal operator and $\mathcal{K}$ stands for complex conjugation.

The spectrum of the above Hamiltonian can be obtained straightforwardly to be

$$E(\boldsymbol{k}) = \beta^2+(\alpha_x^2+\alpha_y^2)+\delta^2+c^2 \pm 2\sqrt{(\alpha_x^2+\alpha_y^2)\delta^2+\alpha_x^2c^2}, \tag{3}$$

where we have introduced short-hand notations: $\beta = 2b(2-\cos k_x-\cos k_y)-\lambda$, $\alpha_{x,y} = a\sin k_{x,y}$, $\delta = d\sqrt{(\cos k_x-\cos k_y)^2+\sin^2 k_x\sin^2 k_y}$. The gap is closed only if $\beta=\alpha_y=\delta^2+c^2-\alpha_x^2=0$, that is,

$$\begin{aligned} & k_y=0, \quad \cos k_x = \frac{d^2\pm\sqrt{a^4-c^2a^2-c^2d^2}}{d^2+a^2}, \\ & \qquad \lambda_{1,2} = 2b(1-\cos k_x) = 2b\frac{a^2\mp\sqrt{a^4-c^2a^2-c^2d^2}}{d^2+a^2}; \end{aligned} \tag{4}$$

$$\begin{aligned} \text{or} \quad & k_y=\pi, \quad \cos k_x = \frac{-d^2\pm\sqrt{a^4-c^2a^2-c^2d^2}}{d^2+a^2}, \\ & \qquad \lambda_{3,4} = 2b(3-\cos k_x) = 8b-2b\frac{a^2\pm\sqrt{a^4-c^2a^2-c^2d^2}}{d^2+a^2}. \end{aligned} \tag{5}$$

Let us focus on the $k_y=0$ case, which is close to the Γ point of the Brillouin zone. Let us also assume that $a\gtrsim d\gg c$ for simplicity. Then we find the two band closing events at $\lambda_1\approx\frac{bc^2}{a^2}$ and $\lambda_2\approx\frac{4ba^2}{d^2+a^2}-\frac{bc^2}{a^2}$. As shown in Fig. S1, we verify from the Wilson loop calculations that when $\lambda_1<\lambda<\lambda_2$, the system is $\mathbb{Z}_2$ nontrivial; when $\lambda<\lambda_1$ or $\lambda_2<\lambda<\lambda_3$, the system is $\mathbb{Z}_2$ trivial.

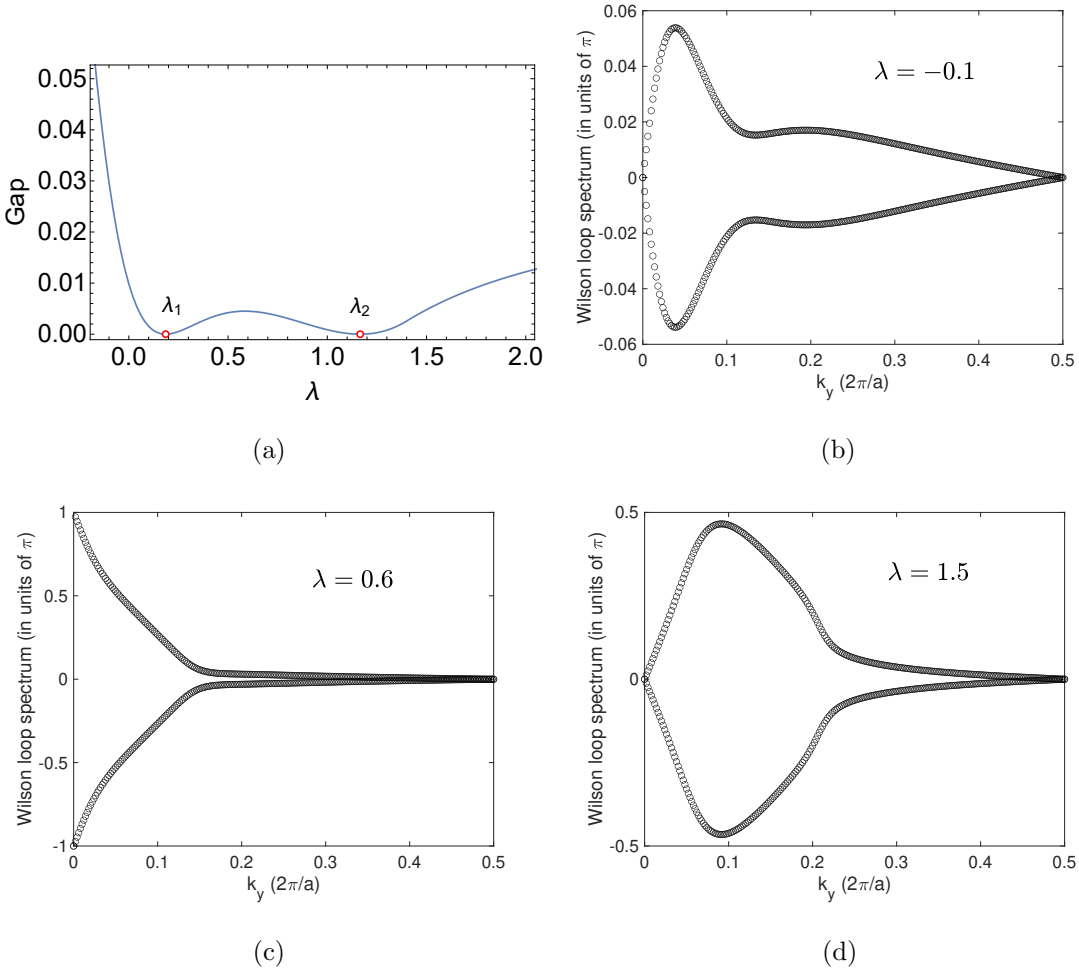

FIG. S2. (a) Numerically obtained band gap as a function of the strength (λ) of band inversion. The two band closing events at $\lambda_{1,2}$ are marked additionally. These two critical λ's separate three phases which are trivial, topological, and trivial, respectively, as verified by Wilson loop calculation results for (b) $\lambda = -0.1$, (c) $\lambda = 0.6$ and (d) $\lambda = 1.5$. The parameters used here are: $b = 1$, $a = 0.5$, $d = 0.7$, $c = 0.2$.

IV. BAND STRUCTURES AND $\mathbb{Z}_2$ CACULATIONS

We report the results of band structure and $\mathbb{Z}_2$ calculations for a few bilayer heterostructures consisted of III_2-VI_3-type 2D ferroelectrics (III = Al, Ga, In; VI = S, Se, Te). The direction of the out-of-plane polarization of each layer is denoted as U for "up polarization" and D for "down polarization", respectively. All these calculations are performed with PBE.

A. In_2Te_3/In_2Se_3

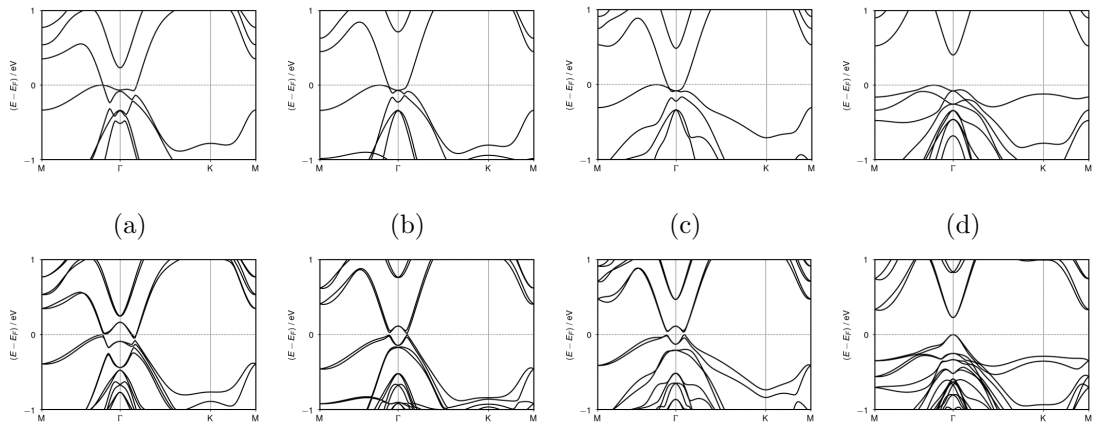

FIG. S3. Band structures for In_2Te_3/In_2Se_3 of four different polarization configurations (a, e) DD, (b, f) DU, (c, g) UD, and (d, h) UU without and with spin-orbit coupling, respectively.

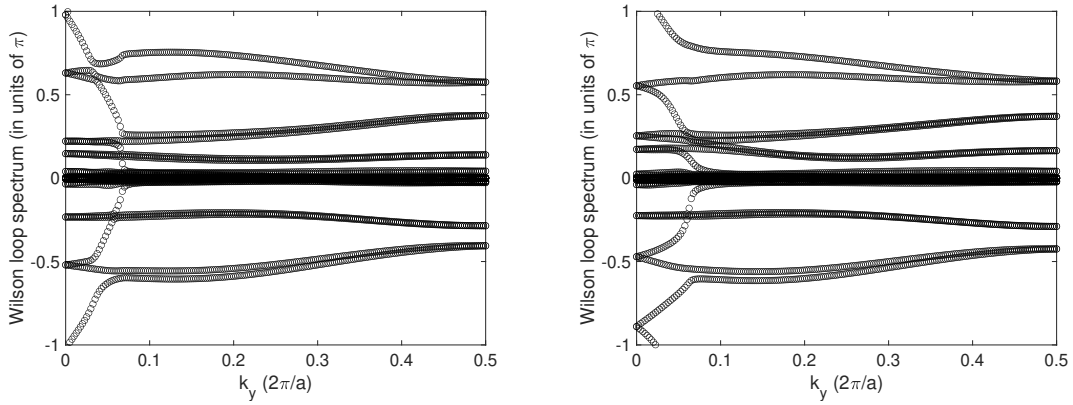

FIG. S4. Wilson loop spectrum for In_2Te_3/In_2Se_3 of (a) DU configuration. $\mathbb{Z}_2 = 1$. (b) UD configuration. $\mathbb{Z}_2 = 1$.

B. Al_2Te_3/Al_2Se_3

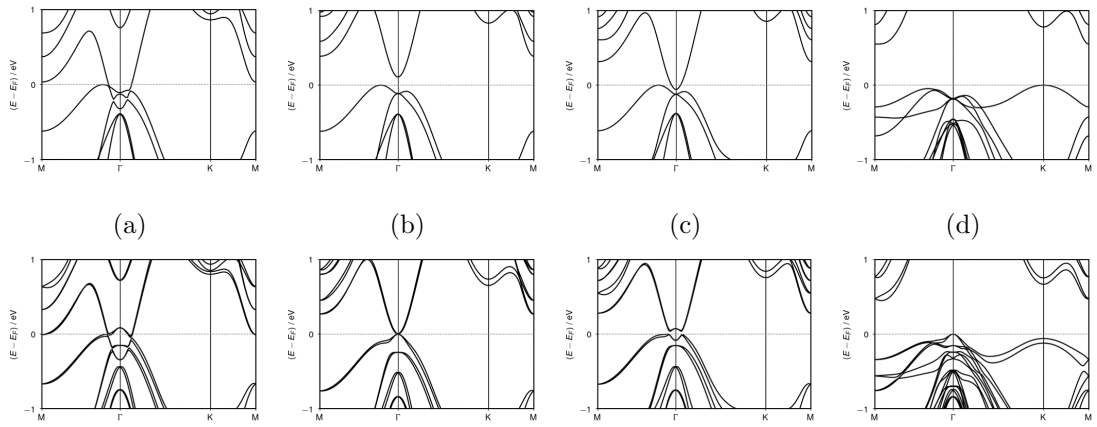

FIG. S5. Band structures for Al_2Te_3/Al_2Se_3 of four different polarization configurations (a, e) DD, (b, f) DU, (c, g) UD, and (d, h) UU without and with spin-orbit coupling, respectively.

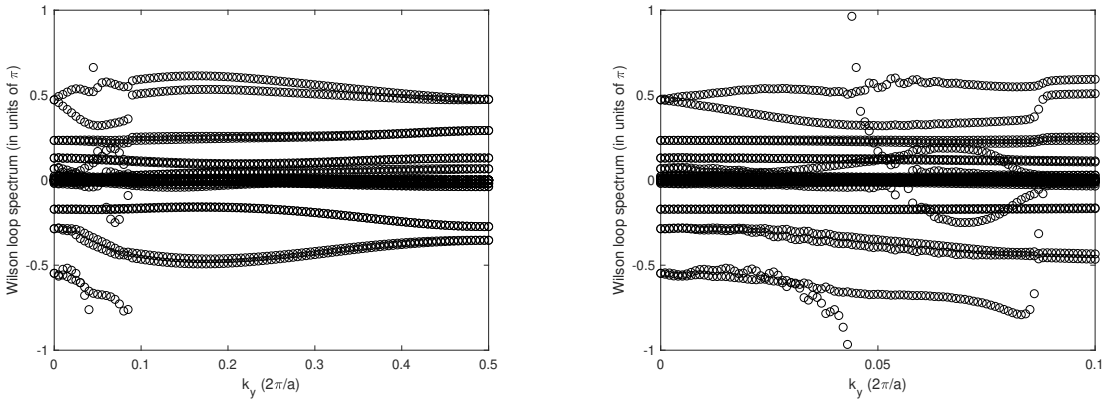

(a) DD

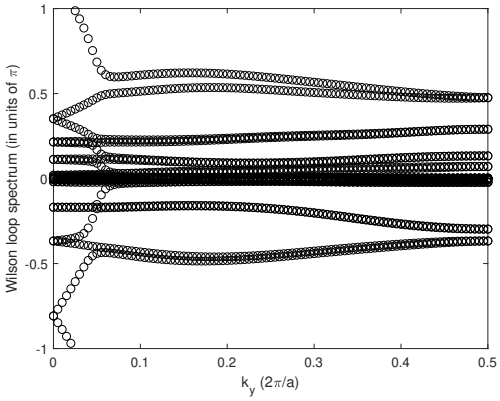

(b) UD

FIG. S6. Wilson loop spectrum for Al_2Te_3/Al_2Se_3 of (a) DD configuration. The figure on the right is a blow-up in the range of $[0, 0.1]$. $\mathbb{Z}_2 = 1$. (b) UD configuration. $\mathbb{Z}_2 = 1$.

C. Al_2Te_3/In_2S_3

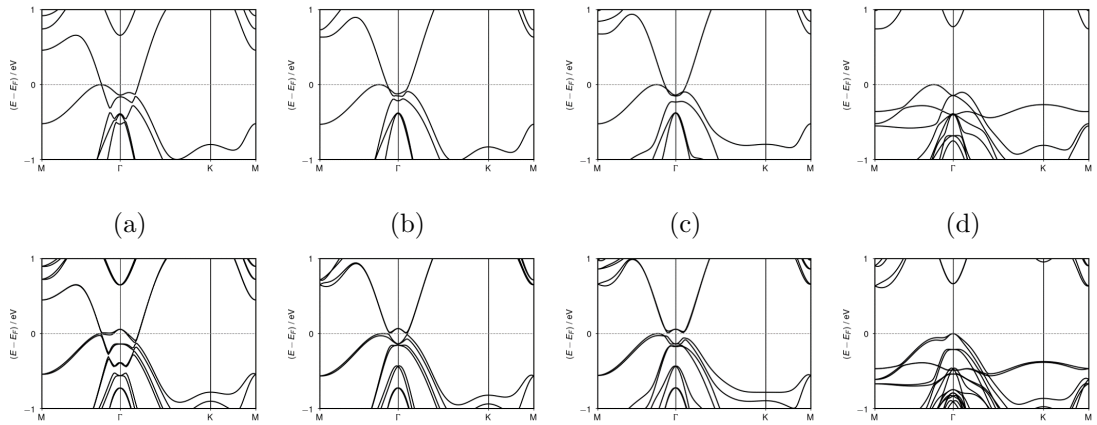

FIG. S7. Band structures for Al_2Te_3/In_2S_3 of four different polarization configurations (a, e) DD, (b, f) DU, (c, g) UD, and (d, h) UU without and with spin-orbit coupling, respectively.

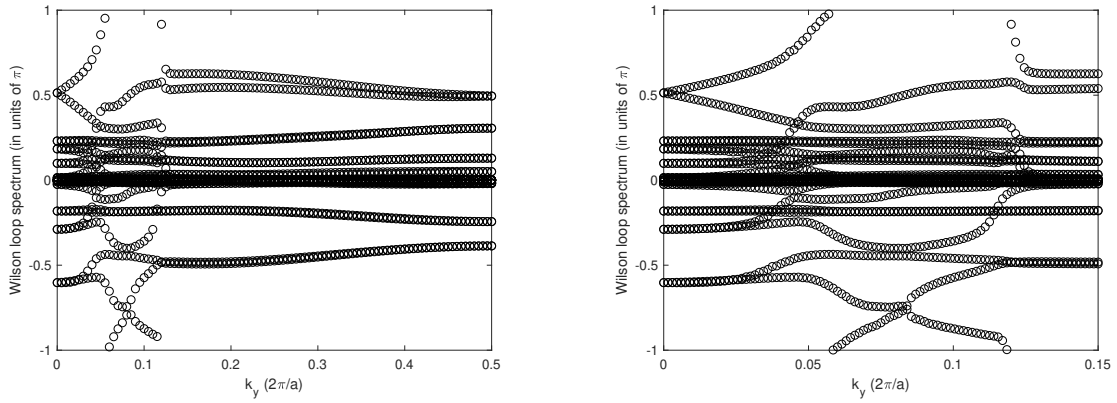

(a) DD

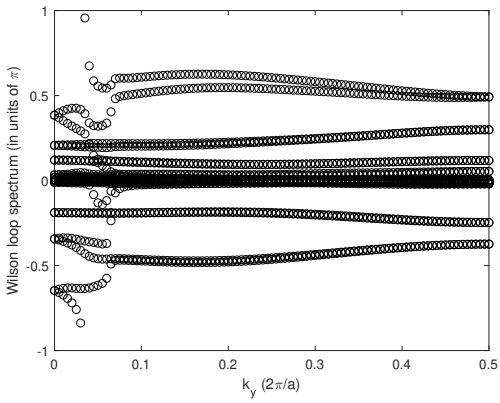

(b) DU

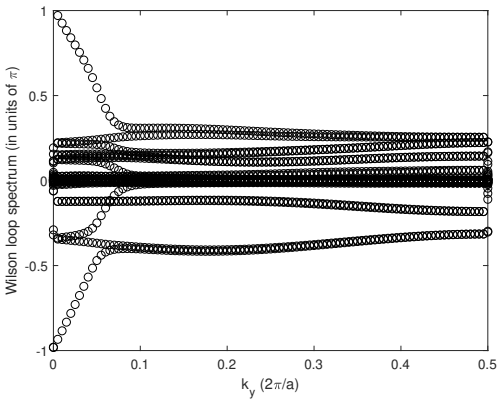

(c) UD

FIG. S8. Wilson loop spectrum for Al_2Te_3/In_2S_3 of (a) DD configuration. The figure on the right is a blow-up in the range of $[0, 0.15]$. $\mathbb{Z}_2 = 0$. (b) DU configuration. $\mathbb{Z}_2 = 1$. (c) UD configuration. $\mathbb{Z}_2 = 1$.

D. Ga_2Se_3/In_2S_3

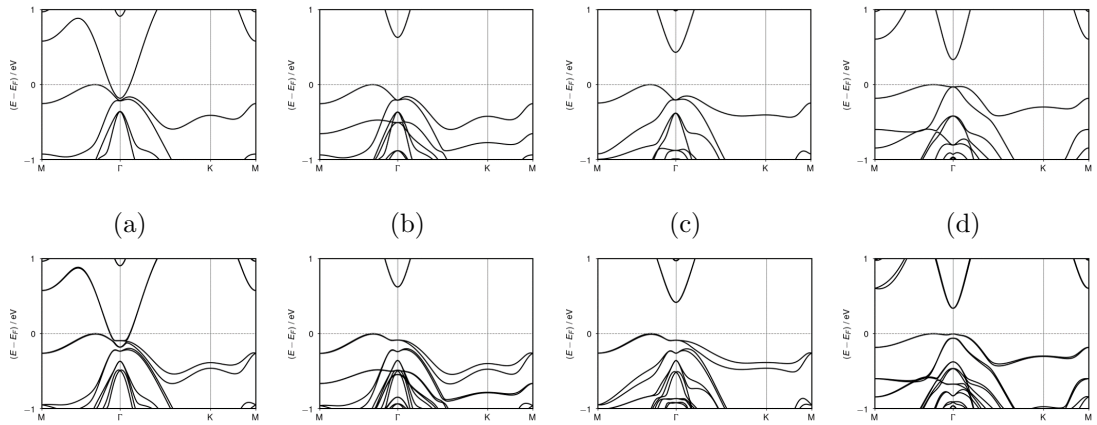

(a) (b) (c) (d)

(e) (f) (g) (h)

FIG. S9. Band structures for Ga_2Se_3/In_2S_3 of four different polarization configurations (a, e) DD, (b, f) DU, (c, g) UD, and (d, h) UU without and with spin-orbit coupling, respectively.

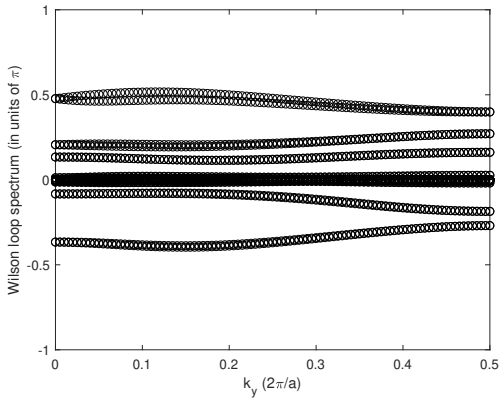

FIG. S10. Wilson loop spectrum for Ga_2Se_3/In_2S_3 of DD configuration. $\mathbb{Z}_2 = 0$.

E. In_2Se_3/In_2S_3

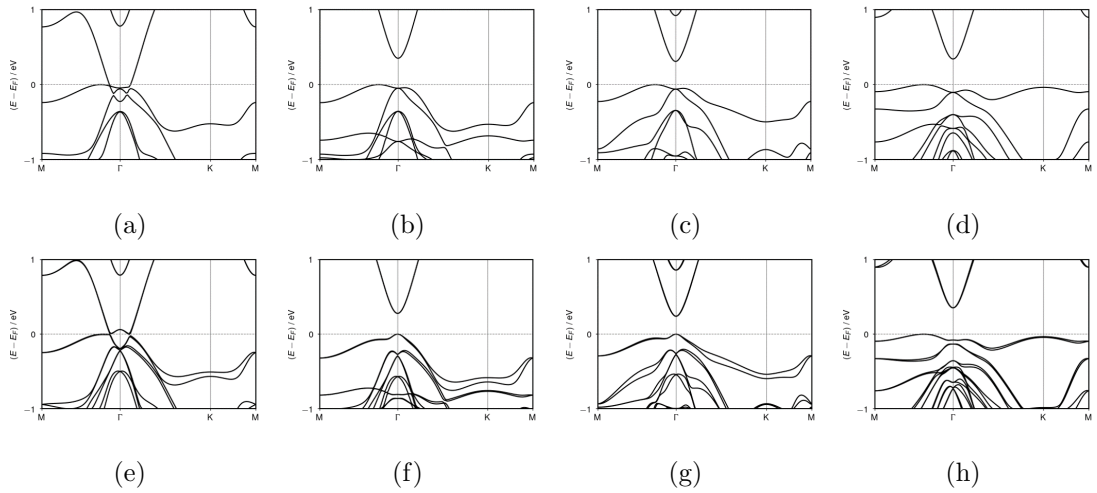

FIG. S11. Band structures for In_2Se_3/In_2S_3 of four different polarization configurations (a, e) DD, (b, f) DU, (c, g) UD, and (d, h) UU without and with spin-orbit coupling, respectively.

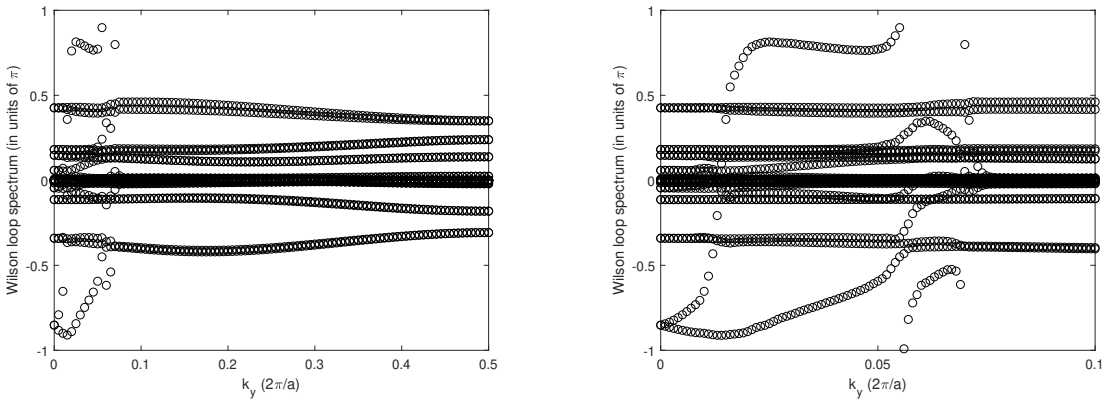

FIG. S12. Wilson loop spectrum for In_2Se_3/In_2S_3 of DD configuration. The figure on the right is a blow-up in the range of $[0, 0.1]$. $\mathbb{Z}_2 = 0$.

F. Al_2Te_3/In_2Se_3

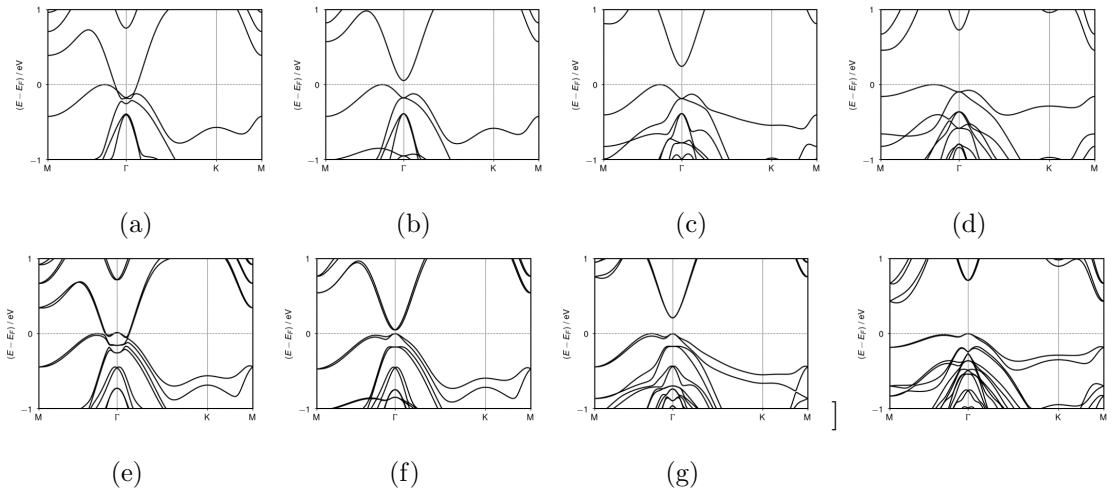

FIG. S13. Band structures for Al_2Te_3/In_2Se_3 of four different polarization configurations (a, e) DD, (b, f) DU, (c, g) UD, and (d, h) UU without and with spin-orbit coupling, respectively.

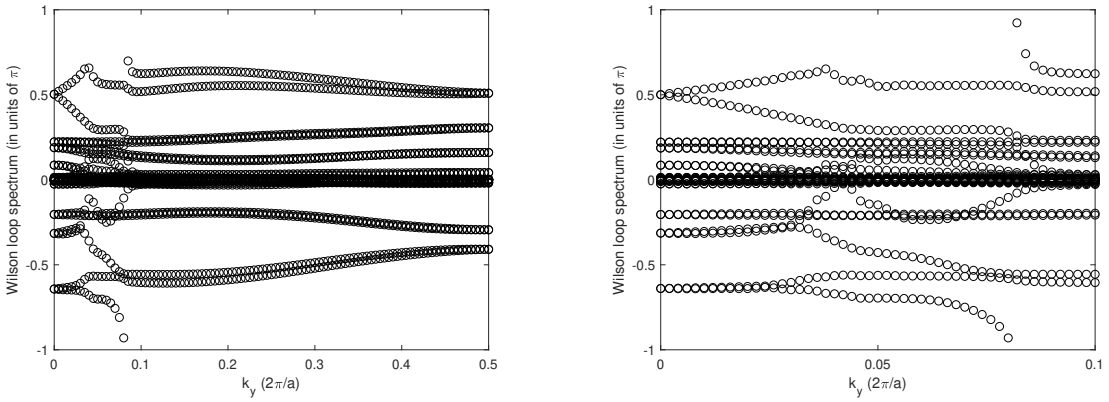

FIG. S14. Wilson loop spectrum for Al_2Te_3/In_2Se_3 of DD configuration. The figure on the right is a blow-up in the range of $[0, 0.1]$. $\mathbb{Z}_2 = 1$.

G. Al_2Se_3/Ga_2S_3

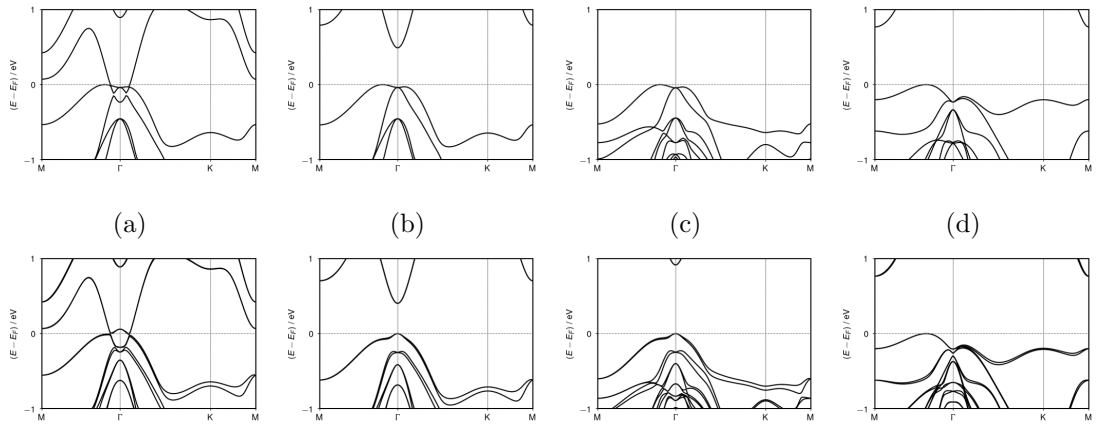

FIG. S15. Band structures for Al_2Se_3/Ga_2S_3 of four different polarization configurations (a, e) DD, (b, f) DU, (c, g) UD, and (d, h) UU without and with spin-orbit coupling, respectively.

V. HSE06 VS PBE BAND STRUCTURES

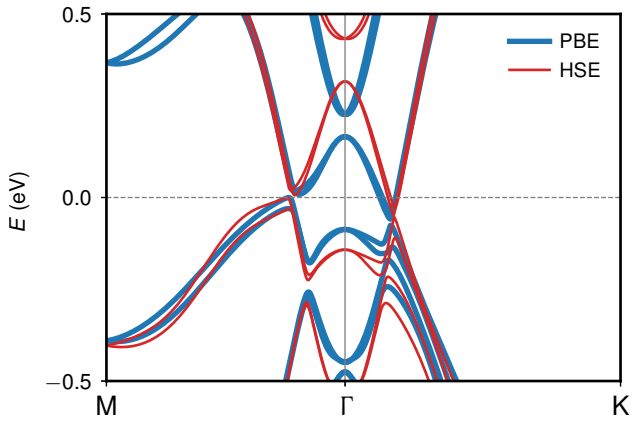

FIG. S16. Comparison of HSE06 and PBE band structures of In_2Te_3/In_2Se_3 of DD configuration. The bands near the Fermi level are comparable.

VI. LAYER RESOLVED DENSITY OF STATES

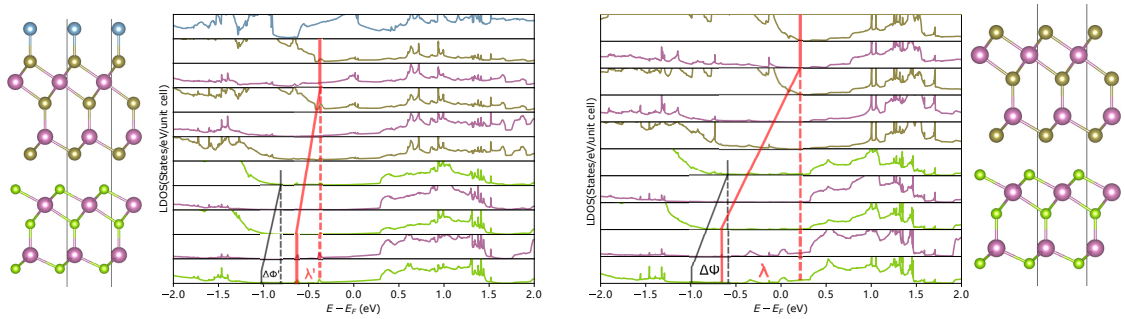

FIG. S17. Comparison of layer resolved density of states of $Al/In_2Te_3/In_2Se_3$ (right) and In_2Te_3/In_2Se_3 (left) of DD configuration. The potential step across the In_2Te_3/In_2Se_3 bilayer becomes smaller after placing the monolayer Al on the top of In_2Te_3 layer.

VII. PHONON SPECTRUM

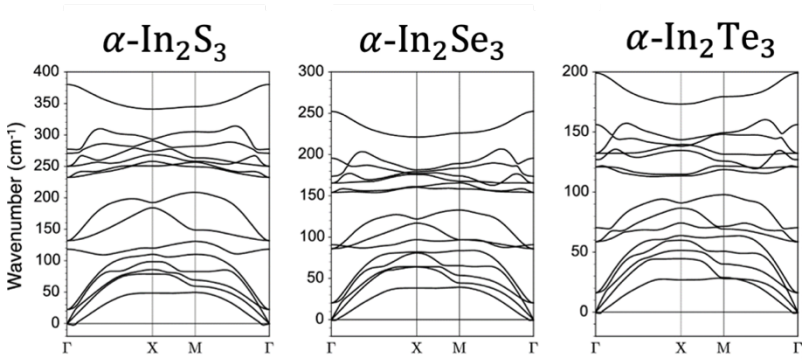

FIG. S18. Phonon spectrums of monolayer α-In_2S_3, α-In_2Se_3, and α-In_2Te_3. Taken from ref.13.

VIII. AIMD SIMULATIONS

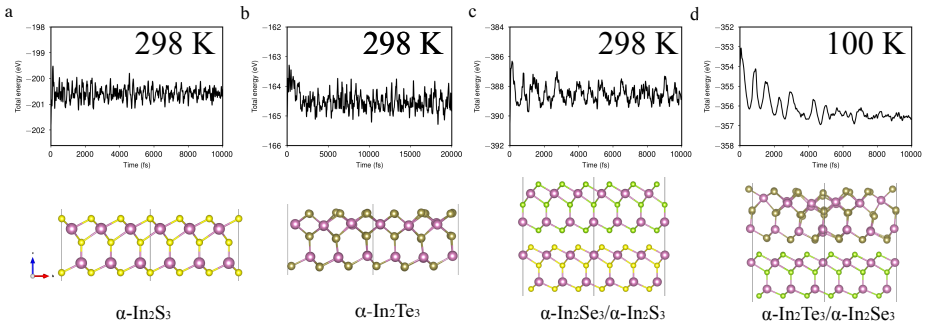

FIG. S19. Ab initio molecular dynamics simulations of α-In_2S_3, α-In_2Te_3, α-In_2Se_3/α-In_2S_3, and α-In_2Te_3/α-In_2Se_3 at finite temperatures. The top panel shows the evolution of potential energy and the bottom panel shows the averaged structure using an equilibrium trajectory of 5 ps. We note that α-In_2Te_3/α-In_2Se_3 undergoes ferroelectric-to-paraelectric phase transition when the temperature is above 100 K. Expectedly, the operating temperature of type-II 2DFETIs should be below its Curie temperature.

The structural stability of α-In_2S_3, α-In_2Te_3, and some bilayer systems is theoretically investigated by performing *ab initio* molecular dynamic (AIMD) simulations implemented in Vienna *ab initio* simulation package [8, 9]. The calculations used the projector augmented wave density functional theory formalism, and the exchange-correlation interaction is described with PBE functional with D3 dispersion correction from Grimme. The plane-wave kinetic energy cutoff is 350 eV and energy convergence criterion is 10^{-5} eV, respectively. A $3 \times 3 \times 1$ supercell is used in AIMD simulations for both monolayer 2D FEs and bilayer heterostructures with Γ-point sampling. The temperature is controlled using the Nosé-Hoover thermostat. The averaged structure is computed using an equilibrium trajectory of 5 ps.

IX. SWITCHING PATHWAYS

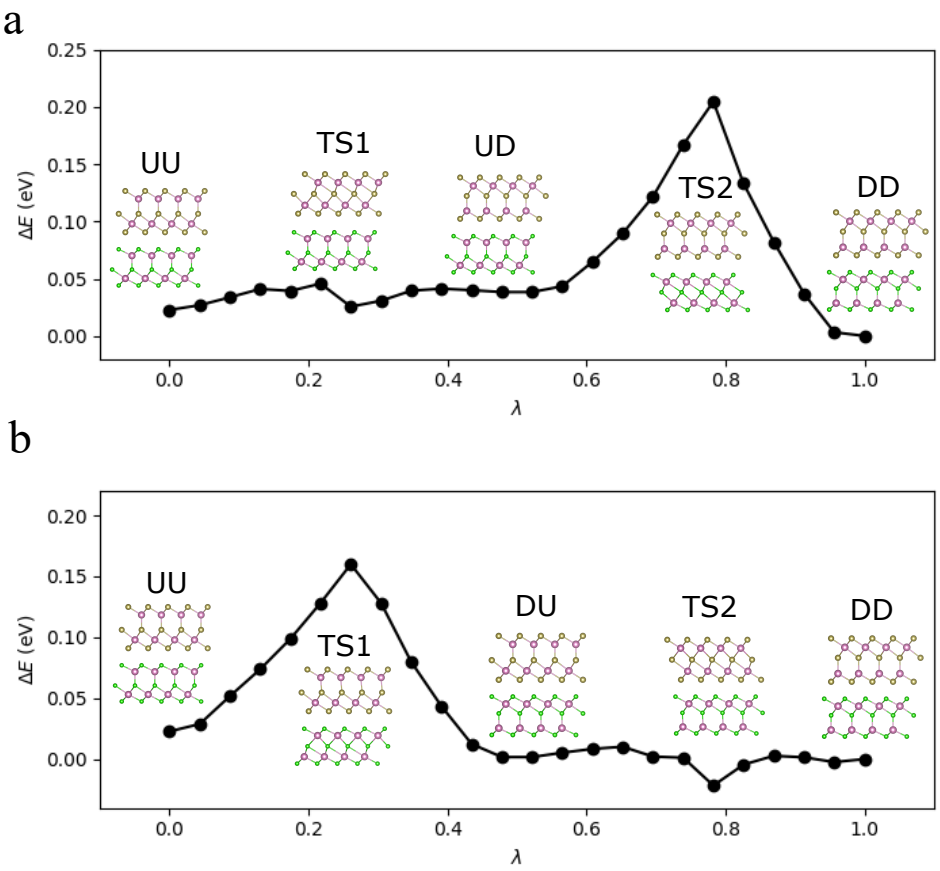

FIG. S20. Two possible out-of-plane polarization reversal pathways for α-In_2Te_3/α-In_2Se_3 bilayer heterostructure.

The minimum energy pathways for 180° out-of-plane polarization reversal in α-In_2Te_3/α-In_2Se_3 bilayer heterostructure is computed using the nudged elastic band (NEB) method. We propose two possible pathways, UU → UD → DD (Fig. S20a) and UU → DU → DD (Fig. S20b). The energy barriers are 0.21 eV and 0.16 eV, respectively, indicating that the bilayer remains swithchable.

[1] S. Grimme, Semiempirical GGA-type density functional constructed with a long-range dispersion correction, J. Comput. Chem. **27**, 1787 (2006).

[2] K. F. Garrity, J. W. Bennett, K. M. Rabe, and D. Vanderbilt, Pseudopotentials for high-throughput DFT calculations, Comput. Mater. Sci. **81**, 446 (2014).

[3] A. V. Krukau, O. A. Vydrov, A. F. Izmaylov, and G. E. Scuseria, Influence of the exchange screening parameter on the performance of screened hybrid functionals, J. Chem. Phys. **125**, 224106 (2006).

[4] M. van Setten, M. Giantomassi, E. Bousquet, M. Verstraete, D. Hamann, X. Gonze, and G.-M. Rignanese, The PseudoDojo: Training and grading a 85 element optimized norm-conserving pseudopotential table, Comput. Phys. Commun. **226**, 39 (2018).

[5] D. R. Hamann, Optimized norm-conserving vanderbilt pseudopotentials, Phys. Rev. B **88**, 085117 (2013).

[6] N. Marzari, A. A. Mostofi, J. R. Yates, I. Souza, and D. Vanderbilt, Maximally localized wannier functions: Theory and applications, Rev. Mod. Phys. **84**, 1419 (2012).

[7] G. Pizzi, V. Vitale, R. Arita, S. Blügel, F. Freimuth, G. Géranton, M. Gibertini, D. Gresch, C. Johnson, T. Koretsune, J. Ibañez-Azpiroz, H. Lee, J.-M. Lihm, D. Marchand, A. Marrazzo, Y. Mokrousov, J. I. Mustafa, Y. Nohara, Y. Nomura, L. Paulatto, S. Poncé, T. Ponweiser, J. Qiao, F. Thöle, S. S. Tsirkin, M. Wierzbowska, N. Marzari, D. Vanderbilt, I. Souza, A. A. Mostofi, and J. R. Yates, Wannier90 as a community code: new features and applications, J. Phys.: Condens. Matter. **32**, 165902 (2020).

[8] G. Kresse and F. J, Efficient iterative schemes for ab initio total-energy calculations using a plane-wave basis set, Phys. Rev. B **54**, 11169 (1996).

[9] G. Kresse and F. J, Efficiency of ab-initio total energy calculations for metals and semiconductors using a plane-wave basis set, Comput. Mater. Sci. **6**, 15 (1996).